Anomalous Hall effect in the coplanar antiferromagnetic coloring-triangular lattice

A. C. Duran [1], S. A. Osorio,[2] and M. B. Sturla[1]

[1]*Instituto de Física de Líquidos y Sistemas Biológicos, CCT La Plata, CONICET and Departamento de Física, Facultad de Ciencias Exactas, Universidad Nacional de La Plata, Casilla de Correo 67, 1900 La Plata, Argentina*

[2]*Instituto de Nanociencia y Nanotecnología, CNEA-CONICET, Centro Atómico Bariloche, R8402AGP, San Carlos de Bariloche, Río Negro, Argentina*

We study the anomalous Hall effect on the antiferromagnetic coloring-triangular lattice with a coplanar magnetic configuration in the presence of a spin-orbit interaction. The effect of the spin-orbit coupling is included at an effective level as a rotation of the electronic spin as the electrons hop from site to site. Our result reveals that a finite Hall conductivity in the planar 120° structure takes place if a finite spin-orbit coupling is present. A quantized Hall conductivity occurs at global band gaps resulting from the topologically nontrivial band structure.

I. INTRODUCTION

The anomalous Hall effect (AHE) is characterized by the presence of a Hall conductivity in the absence of an external magnetic field, in systems where the time-reversal symmetry is broken, as, for example, in magnetic states with net magnetization. But even in the absence of an external field and net magnetization, the Hall phenomena can be observed. In noncollinear magnetic textures, like ferromagnetic and antiferromagnetic skyrmion lattices [1–4], the so-called topological Hall effect [1] (THE) can be observed. Despite their distinctive features, in both cases the Hall phenomena can be described by a nontrivial Berry phase acquired by the electronic states, which leads to a nonzero Berry curvature. In the AHE the underlying physics can be described as a consequence of a reciprocal-space Berry curvature, while in the case of the THE the underlying physics can be described as a consequence of a real-space Berry curvature.

When the magnetic configuration corresponds to coplanar structure with no net magnetization it is not obvious that a Hall effect can take place. The coplanar configuration seems to fail at generating a real-space Berry curvature, as well as the lack of net magnetization fails at generating a Berry curvature in the reciprocal space.

However, it is well known that certain frustrated magnets with coplanar noncollinear states, such as Mn_3Sn [5] and Mn_3Ge [6], exhibit a large value for the Hall conductivity [7–9]. Here, as in the case of a collinear state, the spin-orbit coupling (SOC) plays a central role in the electronic properties of these systems and in particular in the Hall conductivity.

The AHE in coplanar antiferromagnets suggests the presence of a Berry curvature associated with the SOC. Indeed, it turns out that the effect of the SOC can be interpreted in terms of an effective magnetization configuration with a net contribution to the Berry curvature [10].

Recently, Zhang *et al.* [11] have shown that, by introducing the SOC at an effective level in the hopping amplitudes, a direct contribution to the Berry phase in the reciprocal space can be obtained, leading to a nonzero Berry curvature when the SOC is adequately chosen. The effect of the SOC is taken into account by a proper change of the hopping terms. To this end they introduce a set of SU(2) rotation matrices $U_{i,j}$ that take into account the rotation induced by the SOC when the electrons hop between sites i and j.

In this work, we show that an AHE can emerge on a triangular lattice with a coplanar magnetic configuration and no net magnetization. The existence of spontaneous Hall effect on a triangular lattice in the absence of net magnetization has been reported previously for the case of noncoplanar magnetic structure in Ref. [12], which gives rise to a THE. In the present case, we show that a triangular lattice with nonuniform nearest-neighbor hoppings and SOC, in the absence of net magnetization and with a coplanar magnetic structure, can also exhibit a spontaneous Hall effect, but in this case an AHE. We consider a particular pattern of nearest-neighbor hoppings that can be mapped to a three-colored triangular tessellation, generally called color-triangular (CT) lattices. These CT lattices can exhibit a band structure quite similar to that of the kagome lattice [13]. As is well known, many interesting phenomena are attached to the kagome lattice, such as frustration, Dirac cones, and flat bands, which are the scenario for strongly correlated phases [14–21]. Due to the aforementioned connection, many of these phenomena are expected to be present in the CT lattices. Recently, it was shown that the organic compound Cu-dicyanobenzene, which presents the structure of the CT lattice and a ferromagnetic state, exhibits the AHE [22]. In this system, a band structure with nontrivial Berry curvatures emerges as a consequence of a net magnetized state, the presence of SOC, and the similarity with its kagome partner. To the best of our knowledge, the antiferromagnetic counterparts of these CT lattices have not been well studied and are the main objective of this article. In what follows we show that the AHE could emerge in the 120° coplanar structure without net magnetization, which is

045101-1
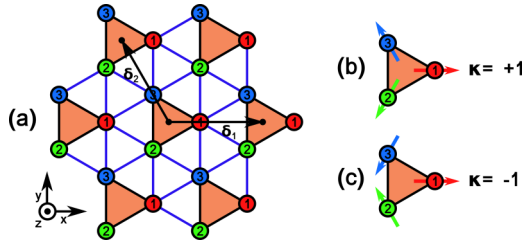
FIG. 1. (a) The triangular lattice with the plaquettes highlighted in orange representing the magnetic cell. The intracell links (black links) include the t_1 hopping and the SOC, while the intercell links correspond to the t_2 hopping. The spins on each site are labeled by 1, 2, and 3. The vectors $\boldsymbol{\delta}_{1,2}$ represent the primitive lattice vectors of the Bravais lattice. For the $120°$ structure [panels (b) and (c)], two possible chiralities are compatible with this magnetic ordering.

characteristic of the triangular antiferromagnets. In the model discussed here, proper combinations of the hopping strengths and, crucially, the SOC lead to a significant contributions to the AHE even in the absence of a ferromagnetic order. As we show here, in this model the interplay between SOC and inhomogeneous hopping integrals leads to the appearance of topologically nontrivial bands. Moreover, for a suitable set of parameters a significant contribution to the Hall conductivity is present. We show that, as a consequence of the presence of topologically nontrivial bands with a definite Chern number, a quantized AHE takes place within the global band gaps.

The article is organized as follows. In Sec. II we introduce the model under study and its band structure. In Sec. III we analyze the band topology and deliver the main results on the Hall conductivity and the presence of chiral edge states. In Sec. IV we discuss possible experimental realizations of the model as considered here. Finally, in Sec. V we summarize our main results and conclusions.

II. THE MODEL AND BAND STRUCTURE

The model consists of a two-dimensional triangular lattice with a lattice spacing a. The magnetic cell is comprised of three sites where the spins lie in the plane of the system forming a $120°$ structure (Fig. 1). The bonds connecting two sites within a magnetic cell [black lines in Fig. 1(a)] are characterized by the hopping amplitude t_1 and the SOC, whereas the bonds connecting sites between adjacent magnetic cells are characterized by a hopping amplitude t_2 without SOC [blue lines in Fig. 1(a)]. The effect of the magnetic texture is taken into account via a Hund's coupling between the electronic spin and the localized magnetic moments. The SOC is treated here in the context of an effective theory as discussed in Ref. [11]. The Hamiltonian then reads as follows:

$$
\begin{aligned}
\mathcal{H} &= \mathcal{H}_t + \mathcal{H}_J, \\
\mathcal{H}_t &= \sum_{\langle j,k \rangle} (t_{kj} \mathbf{c}_k^\dagger U_{kj} \mathbf{c}_j + t_{kj}^* \mathbf{c}_j^\dagger U_{kj}^\dagger \mathbf{c}_k), \\
\mathcal{H}_J &= -\frac{JS}{2} \sum_j \mathbf{c}_j^\dagger \boldsymbol{\sigma} \mathbf{c}_j \cdot \mathbf{n}_j.
\end{aligned}
\tag{1}
$$

The $\mathbf{c}_j$ and $\mathbf{c}_j^\dagger$ are two-component spinors:

$$
\mathbf{c}_j = \begin{pmatrix} c_{j,\uparrow} \\ c_{j,\downarrow} \end{pmatrix}, \quad \mathbf{c}_j^\dagger = (c_{j,\uparrow}^\dagger, c_{j,\downarrow}^\dagger).
$$

The localized spin on site j is represented by the vector $\mathbf{n}_j$, which takes three possible values leading to a tripartite lattice as shown in Fig. 1. The SOC is introduced effectively in the SU(2) matrix U_{kj} through two parameters for each bond connecting the sites k and j. Since U_{kj} represents a rotation of the electronic spin we can write it in terms of a unit vector, $\mathbf{a}_{kj}$, that gives the direction of the rotation and the rotation angle α_{kj} (that measures the SOC strength):

$$
U_{kj} = \exp\left[-\frac{i\alpha_{kj}}{2} (\mathbf{a}_{kj} \cdot \boldsymbol{\sigma}) \right],
\tag{2}
$$

where $\boldsymbol{\sigma} = (\sigma_x, \sigma_y, \sigma_z)$ is a vector of Pauli matrices. In this effective approach the direction of the vectors $\mathbf{a}_{kj}$, which characterize the SOC, can be inferred following the rules for the Dzyaloshinskii-Moriya interaction (DMI) [23]. According to these rules, the mirror plane $\mathcal{M}_z$ parallel to the lattice plane would set the unit vectors $\mathbf{a}_{kj}$ to be perpendicular to the lattice plane, but we consider the lattice to be embedded in a three-dimensional structure which breaks this $\mathcal{M}_z$ symmetry. The presence of a mirror symmetry plane, $\mathcal{M}_i$, perpendicular to each black bond in Fig. 1 and passing through its midpoint sets the vectors $\mathbf{a}_{kj}$ to be parallel to $\mathcal{M}_i$ in such bonds. Thus, we choose the vectors $\mathbf{a}_{kj}$ to point to the outer region of the triangular plaquette and $\mathbf{a}_{kj} \perp \hat{\mathbf{r}}_{kj}$, where $\hat{\mathbf{r}}_{kj}$ points in the direction of the intracell bond connecting the sites k and j [black lines in Fig. 1(a)], that is,

$$
\begin{aligned}
\mathbf{a}_{12} &= \frac{1}{2}\cos(\phi)\hat{x} - \frac{\sqrt{3}}{2}\cos(\phi)\hat{y} + \sin(\phi)\hat{z}, \\
\mathbf{a}_{23} &= -\cos(\phi)\hat{x} + \sin(\phi)\hat{z}, \\
\mathbf{a}_{13} &= \frac{1}{2}\cos(\phi)\hat{x} + \frac{\sqrt{3}}{2}\cos(\phi)\hat{y} + \sin(\phi)\hat{z},
\end{aligned}
$$

where ϕ is the angle between the vectors $\mathbf{a}_{ij}$ and the lattice plane.

Up to now this model corresponds to the general CT lattice and could be the scenario for a wide variety of phenomena if we consider different setups for the parameters. However, we limit ourselves to a particular case. We consider $|t_1| \leqslant |t_2|$. The reason for this is twofold. On one side, we found that for $|t_1| > |t_2|$ the Hall conductivity is strongly suppressed even in the presence of a SOC as shown in Fig. 4. On the other side, the setup with $|t_1| \leqslant |t_2|$ has the potential to describe real systems as we discuss in Sec. IV.

While the band structure changes with the value of ϕ, the topological characteristics of each band remains unchanged, so, for concreteness, we set $\phi = 0$ for the rest of the article. This situation can reproduce the emergent SOC due to inversion symmetry breaking in real systems (discussed in Sec. IV).

The $120°$ magnetic configuration is degenerated for the case of an inversion-symmetric antiferromagnet with pure exchange interactions. This degeneracy corresponds to the two possible chiralities for the $120°$ structure [Figs. 1(b) and 1(c)]. However the presence of an antisymmetric interaction such as the DMI can lift this degeneracy and select a state with definite

chirality. For the present case we assume that the magnetic configuration corresponds to that shown in Fig. 1(b).

We describe the properties of this model through the Hamiltonian in Eq. (1), which in momentum space is a 6×6 matrix given by

$$
\mathcal{H}_{\mathbf{k}} = \begin{pmatrix} -\frac{JS}{2}\boldsymbol{\sigma}\cdot\mathbf{n}_1 & H_{12}^{\dagger} & H_{13} \\ H_{12} & -\frac{JS}{2}\boldsymbol{\sigma}\cdot\mathbf{n}_2 & H_{23}^{\dagger} \\ H_{13}^{\dagger} & H_{23} & -\frac{JS}{2}\boldsymbol{\sigma}\cdot\mathbf{n}_3 \end{pmatrix}, \quad (3)
$$

with

$$
H_{13} = t_1 U_{13} + t_2(e^{-i\mathbf{k}\cdot(\delta_1+\delta_2)} + e^{-i\mathbf{k}\cdot\delta_2}),
$$

$$
H_{12} = t_1 U_{12} + t_2(e^{-i\mathbf{k}\cdot(\delta_1+\delta_2)} + e^{-i\mathbf{k}\cdot\delta_1}),
$$

$$
H_{23} = t_1 U_{23} + t_2(e^{-i\mathbf{k}\cdot\delta_2} + e^{i\mathbf{k}\cdot\delta_1}),
$$

and $\delta_{1,2}$ are the primitive lattice vectors of the Bravais lattice as depicted in Fig. 1. We arrive at Eq. (3) by writing the Hamiltonian in Eq. (1) in terms of the operators c_i, replacing the sum $\sum_i$ over lattice sites by the sum $\sum_{\mathbf{R}} \sum_{\mathbf{r}_\mu(\mu=1,2,3)}$, where $\mathbf{R}$ represents the plaquette positions and $\mathbf{r}_\mu$ represents the position of each site μ with respect to the center of the plaquette. We then Fourier transform $c_{\mathbf{R},\mu}$:

$$
c_{\mathbf{R},\mu} = \frac{1}{\sqrt{N}} \sum_{\mathbf{k}} \exp[i\mathbf{k}\cdot(\mathbf{R}+\mathbf{r}_\mu)]c_{\mathbf{k},\mu}.
$$

Finally we absorb the phase factor $e^{i\mathbf{k}\cdot\mathbf{r}_\mu}$ by introducing new operators $\tilde{c}_{\mathbf{k},\mu} = e^{i\mathbf{k}\cdot\mathbf{r}_\mu}c_{\mathbf{k},\mu}$.

The most general electronic structure consists of six bands that, for $J = 0$ and $\alpha = 0$, merge into a lower number of degenerated bands. We study some particular limits of the previous model and, in order to do that, we consider $t_1 + t_2 = 1$ and parametrize the imbalance between them as $t_1 = (1+\lambda)/2$ and $t_2 = (1-\lambda)/2$, with $-1 \leqslant \lambda \leqslant 1$. In the first place we have the case $\lambda = 1$ ($t_2 = 0$). In this situation the system consists of a series of independent triangular plaquettes; this leads to electronic states localized at each plaquette. In fact the band structure corresponds to two flat bands: the upper band is doubly degenerated and the lower band has a fourfold degeneracy. For $0 < \lambda < 1$ the lower band splits into two bands with two crossing points at the Γ and K points. However, they remain well separated from the upper band. A gap closing for $\lambda = 0$ ($t_1 = t_2$) introduces additional crossings, now between the upper and lower bands.

On the opposite side $\lambda = -1$ ($t_1 = 0$), and for $J = 0$ and $\alpha = 0$, the band structure resembles that of the kagome lattice with three (doubly degenerate) bands and level crossings at the Γ and K points. For $-1 < \lambda < 0$, those band crossings survive and no other crossings are developed insofar as λ belongs within the previous range.

It is important to mention that, since in the model considered here the SOC acts through the t_1 terms, in the limit $t_1 = 0$ the SOC has no effect on the band structure irrespective of the value of J. Out of this limit, the introduction of the Hund's coupling and the SOC can induce a band structure in which all bands are well separated from each other. In the next section we study this regime, that is, $-1 < \lambda < 0$, and discuss the effect of a finite SOC on the Hall conductivity.

III. HALL CONDUCTIVITY

Since the Hall conductivity σ_{xy} is related to the topology of the electronic bands, we start with a topological analysis of the band structure of the system. To this end we consider the Bloch Hamiltonian $\mathcal{H}_{\mathbf{k}}$ in Eq. (3). Without loss of generality, we fix the SOC strength setting as $\alpha = 0.2\pi$ in the rest of the article.

As we mention in the previous section, when we move the values of the parameters some of the gaps are closed and then reopened, signaling a topological phase transition. To characterize this transitions we calculate the Chern numbers C_n, where n labels the bands from the lowest ($n = 1$) to the highest ($n = 6$), associated with each band. The set of Chern numbers can be computed as follows:

$$
C_n = \frac{1}{2\pi i} \int_S \Omega^n(\mathbf{k})d^2k, \quad (4)
$$

where the integral is evaluated on the surface S corresponding to the Brillouin zone. The Berry curvature is expressed in terms of the Berry connection $A_{k_\mu}^n(\mathbf{k})$ for the nth band, with $\mu = x$ and y, through the equations

$$
\Omega^n(\mathbf{k}) = \partial_{k_x}A_{k_y}^n(\mathbf{k}) - \partial_{k_y}A_{k_x}^n(\mathbf{k}), \quad (5)
$$

$$
A_{k_\mu}^n(\mathbf{k}) = \langle n(\mathbf{k})|\partial_{k_\mu}|n(\mathbf{k})\rangle. \quad (6)
$$

The Chern numbers are computed by numerically discretizing the Brillouin zone and computing the Berry phase in each discrete plaquette in k space, following the numerical method developed by Fukui-Hatsugai-Suzuki [24].

As mentioned in the previous section, for positive values of λ ($t_1 > t_2$) the system is topologically trivial; that is, we found $C_n = 0 \ \forall n$. For negative values of λ we found nonzero Chern numbers for the different bands. For example, in Fig. 2 we show the band structure together with the Chern numbers of each band for two representative cases. When the $120°$ structure is uniformly rotated through an angle θ around a vector perpendicular to the plane of the system, the band structure changes. The Hall conductivity for a Fermi level within a band gap behaves as a step function of θ (varying from 1 to -1), similar to the behavior shown in Ref. [10]. Each band retains its nontrivial character regardless of the angle value, although the Chern number sign changes. Thus, without loss of generality, for the magnetic background we keep the structure as depicted in Fig. 1(b).

So far we have seen that the presence of SOC could lead to nontrivial bands for suitable ratios of t_1/t_2. We analyze now the consequences of those results in the anomalous Hall conductivity, which is our ulterior objective. The Hall conductivity σ_{xy} is given by [25]

$$
\sigma_{xy} = \frac{e^2}{(2\pi)h} \int_{\text{B.Z.}} \sum_n f(E_n(\mathbf{k}))\Omega^n(\mathbf{k})d^2k, \quad (7)
$$

where the sum runs over all energy bands and $f(E_n(\mathbf{k}))$ is the Fermi-Dirac distribution. At zero temperature we can approximate $f(E_n(\mathbf{k}))$ by the step function $\Theta[\epsilon_f - E_n(\mathbf{k})]$, with ϵ_f being the Fermi level, and compute the Hall conductivity as a function of ϵ_f for different values of J at fixed values
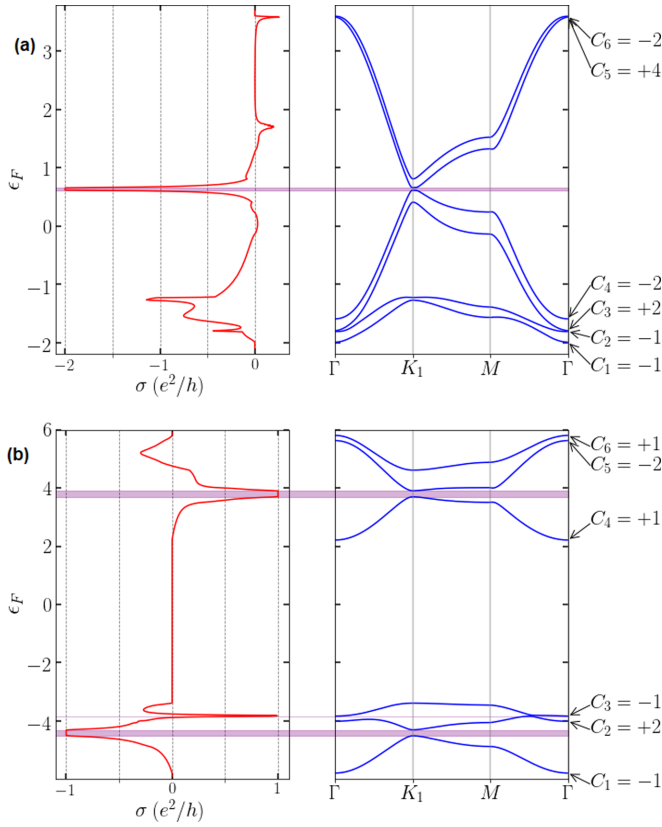
FIG. 2. (a) Hall conductivity and band structure for $\lambda = -0.6$ and $J = 0.4$. One gap is visible in the band structure between bands 4 and 5, which leads to a plateau in the Hall conductivity equal to the accumulated Chern number. All bands have a nonzero Chern number. (b) Hall conductivity and band structure for $\lambda = -0.6$ and $J = 8$. In this case there are three gaps in the band structure, each one leads to its corresponding plateau in the Hall conductivity. All six bands have a nonzero Chern number.

$\lambda = -0.6$ and $\alpha = 0.2\pi$ as seen in Fig. 2 for two representative cases.

We can see that the ingredients considered here could introduce large contributions to the Hall conductivity as a consequence of nontrivial bands. It is interesting to note that even in the weak Hund's coupling regime the Hall conductivity is large. In fact, for small values of J the Hall conductivity could be increased by a factor of 2 as compared with the large J case shown in Fig. 2(b). A quantized Hall conductivity is obtained at the global gaps indicated by the red bars in Fig. 2, $\sigma_{xy} = C \times e^2/h$, where $C = \sum_n C_n$ and the index n runs over the band index up to the last band below the gap under consideration. This quantization of the Hall conductivity is a hallmark of the nontrivial topological structure of the electronic bands and suggests the presence of robust edge states. The magnitude of the plateaus in the Hall conductivity is proportional to the number of chiral edge channels. We therefore expect two homochiral states for the case represented in Fig. 2(a) at $E \approx 0.6$. In the case represented in Fig. 2(b), we have at most one chiral state, and the chirality of the states at $E \approx -3.9$ and $E \approx 3.8$ is opposite to that of the state at $E \approx -4.4$. To show this in this last case, we consider a ribbon of 30 sites long (along the direction $\hat{v} = \frac{\sqrt{3}\hat{x}}{2} + \frac{\hat{y}}{2}$)

and infinitely long in the $\hat{y}$ direction. The band structure for the ribbon is shown in Fig. 3(a). The band structure consists of two band bundles separated by a large band gap. There are three smaller gaps, and within these last gaps we can find the aforementioned edge states. In Fig. 3(b) we show the band structure around the gap at $E \approx 3.8$. The bands crossing the gap connect the upper and lower levels and correspond to the gapless edge states. Each of them are localized at opposite ends of the ribbon as shown in Fig. 3(d) for $k_y/3a = 0.5$. A similar situation is observed for the gap at $E \approx -4.4$ in Fig. 3(c), where we find again a pair of states crossing the gap and they correspond to edge states as seen in Fig. 3(e). In Figs. 3(d) and 3(e) the colors red and blue distinguish the states localized at the right and left edges, respectively, and the intensity of the colors and the size of the points are proportional to the square of the wave function $|\Psi_i|^2$ on each site of the ribbon. We have also computed the polarization of the chiral edge states shown in Figs. 3(d) and 3(e). For the left and right states in Fig. 3(d), we find $\mathbf{S} \approx (0.155, 0, 0.145)$ and $\mathbf{S} \approx (-0.160, 0, -0.163)$, respectively. Analogously, we find $\mathbf{S} \approx (-0.256, 0, 0.118)$ and $\mathbf{S} \approx (0.134, 0, -0.176)$ for the left and right states, respectively, in Fig. 3(e). It is seen that S_y, the polarization along the edge, is zero. Then, the polarization of the edge states is transverse to the propagation direction and lives in the x-z plane; a similar phenomenology is found in the quantum anomalous Hall effect in collinear states [26].

Since for $\lambda > 0$ all the Chern numbers are zero, the absolute value of the Hall conductivity becomes orders of magnitude lower than the $\sigma(\epsilon_f)$ obtained for $\lambda < 0$, as seen in Fig. 4. A different situation arises when we turn off the spin-orbit coupling by setting $\alpha = 0$, in this case both $C_n = 0 \,\forall n$ and $\sigma_{xy}(\epsilon_f) = 0$ (see Fig. 4, blue line), which evidences the relevance of a finite SOC.

In Fig. 5 we show a phase diagram representing the different values of the vectors of Chern numbers $\bar{C} = (C_1, C_2, C_3, C_4, C_5, C_6)$ in the J-λ space for $0.4 < J < 2$ and $-1 < \lambda < 0$. We concentrate on negative values of λ since, as was previously discussed, all the Chern numbers for $\lambda > 0$ are zero. Each region maps a different set of Chern numbers for each band.

IV. POSSIBLE REALIZATION IN REAL SYSTEMS

Besides the cases discussed previously, we have seen that even for the case of $t_1 = t_2$ the Hall conductivity exhibits a strong plateau. This brings the possibility to realize the anomalous Hall effect in a conventional triangular antiferromagnet, provided the SOC can suitably be introduced on each triangular plaquette. This effect can be induced by the adsorption of transition metal atoms sitting on the lattice sites and voids of a transition metal dichalcogenide monolayer and forming a triangular arrangement. In Ref. [27] this process actually leads to a DMI between the magnetic moments that forms a triangular antiferromagnetic lattice. Thus we expect that the SOC, as considered here, can be induced by this mechanism. Following the previous line, the more generic CT lattice (with $t_1 \neq t_2$) can be achieved by the same mechanism of adsorption. This was considered in Ref. [13]. The authors showed that Au atoms adsorbed onto a monolayer of the
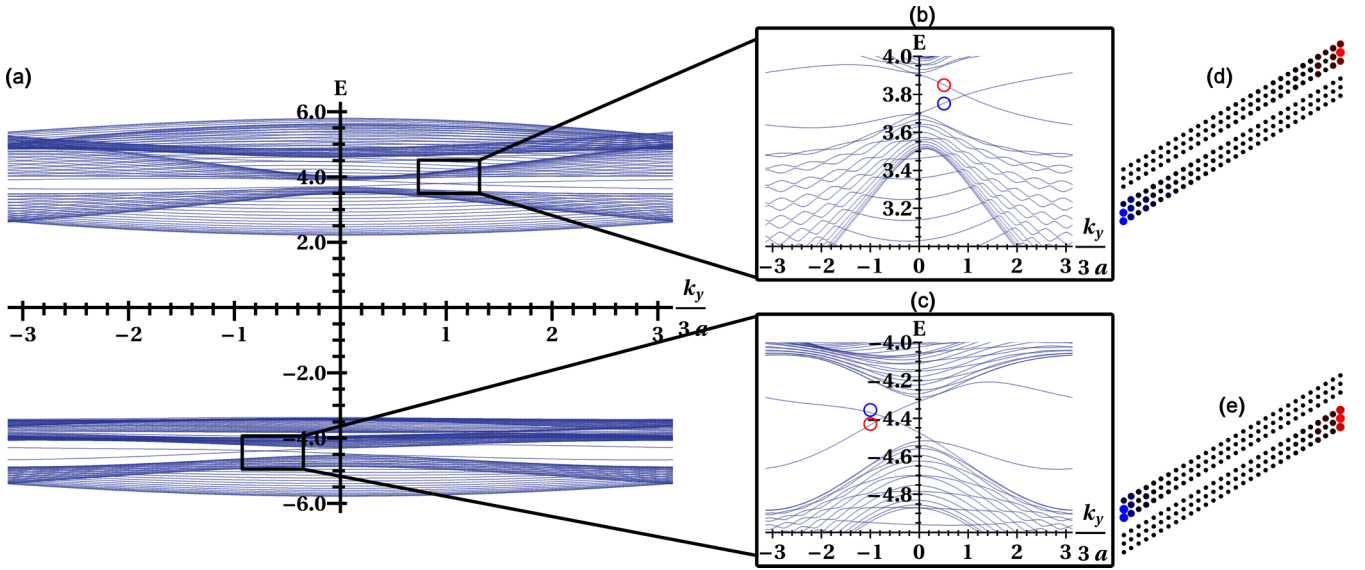
FIG. 3. (a) The band structure of a ribbon that is 30 sites long for $\lambda = -0.6$, $J = 8$, and $\alpha = 0.2\pi$. Detail of the band structure showing the edge states at (b) the upper band gap (around $E \approx 3.8$) and (c) the lower band gap (around $E \approx -4.4$). The blue and red circles [at $k_y/3a = 0.5$ in panel (b) and $k_y/3a = -1$ in panel (c)] correspond, respectively, to the left and right edge states represented for the upper (d) and lower (e) band gaps. In panels (d) and (e), the size of the circles and the intensity of the color, red (for right edges) and blue (for left edges), indicate the square of the wave amplitude at the corresponding site on the ribbon.

compound Ca_2N lead to a band structure that has the structure of the kagome bands, and this requires $|t_1| < |t_2|$ in the CT lattice partner.

The magnetization configuration (the $120°$ state) considered here is characteristic of several frustrated antiferromagnets. In particular, the triangular antiferromagnetic lattice exhibits this state as a ground state. However, in the pure Heisenberg Hamiltonian with only exchange interactions, there are many states within this class of configuration. In addition to the SO(3) global symmetry, which corresponds to the different orientations of the planar magnetic configuration, there is an additional degree of freedom, namely, the chirality. This property further distinguishes the $120°$ state to belong in two classes as shown in Figs. 1(b) and 1(c). For the pure Heisenberg Hamiltonian the two chiralities are degenerated. However, the chirality selection can occur due to chiral interactions such as the DMI. This kind of process could take place, for example, in the triangular antiferromagnet $Ba_3NbFe_3Si_2O_{14}$ [28]. It is important to mention that in a recent article the authors claim that the DMI is not strong enough to lift the chirality degeneracy [29].
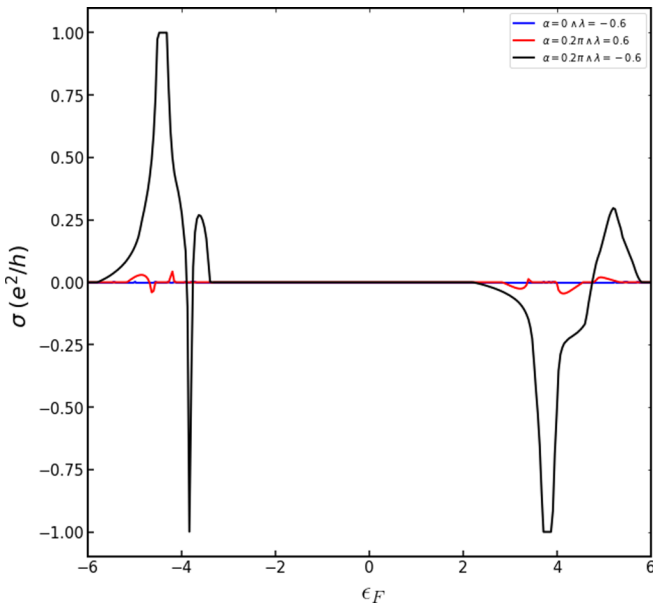
FIG. 4. Hall conductivity for three different configurations of the parameters λ and α but with a set Hund's coupling $J = 8$. When the SOC strength is set to $\alpha = 0$, the Hall conductivity is null. If we increase the SOC strength, the Hall conductivity becomes nonzero, but acquires significant values only for $\lambda \leqslant 0$, which corresponds to $t_2 \geqslant t_1$.
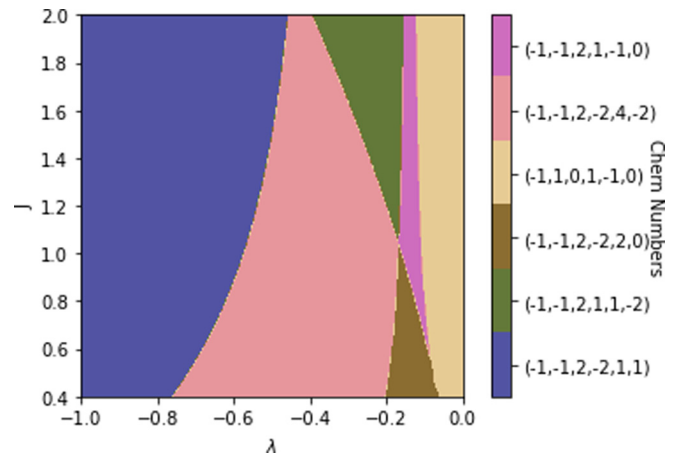
FIG. 5. A phase diagram in the J-λ space for $0.4 < J < 2$ and $-1 < \lambda < 0$. We concentrate on negative values of λ since all the Chern numbers for $\lambda > 0$ are zero. Each colored region maps a different set of Chern numbers for each band.

Thus, the different and key ingredients of our model are present in actual electronic and magnetic systems. So far, we have considered them as separated components and spread over a wide range of materials. Reuniting them into a single compound can be challenging, since these ingredients can appear entangled in a real system, which possibly can make it difficult to obtain a representative material consistent with our model. However, as we mentioned earlier, the emergent band structure of the CT lattice resembles that of the kagome lattice (in fact, by setting $t_1 = 0$ the band structure of the kagome lattice is recovered), which provides an alternative scenario in which the previous ingredients could be disentangled and effectively realize the CT lattice as considered here [13].

V. CONCLUSIONS

We have studied the anomalous Hall effect on a CT lattice antiferromagnet and have shown that a strong anomalous Hall effect is present in a coplanar magnetic texture without net magnetization. The SOC is at the heart of this phenomena since, for the system without SOC, the Hall conductivity is inhibited. Another key ingredient is the different values for the intraplaquette (t_1) and the interplaquette (t_2) hoppings. When the former is weaker than the latter, a strong Hall conductivity emerges. The other way around, for $t_1 > t_2$, the Hall conductivity is strongly suppressed.

The results discussed here reveal that the CT lattice provides an excellent playground for the anomalous Hall effect even in the antiferromagnetic case with a coplanar magnetic configuration. As such, we expect that the phenomena described here could be realized in the systems previously discussed, from which we highlight the antiferromagnetic organic compounds with the structure of the CT lattice and the triangular antiferromagnetic systems formed with transition metal atoms adsorbed onto a transition metal dichalcogenide monolayer. In view of the similarity between the band structure of the kagome lattice and the CT lattice, the latter also provides an excellent playground for studying the interplay between strong correlations and topology in electronic systems.

ACKNOWLEDGMENTS

[1] N. Nagaosa and Y. Tokura, Nat. Nanotechnol. **8**, 899 (2013).

[2] H. D. Rosales, D. C. Cabra, and P. Pujol, Phys. Rev. B **92**, 214439 (2015).

[3] S. A. Osorio, H. D. Rosales, M. B. Sturla, and D. C. Cabra, Phys. Rev. B **96**, 024404 (2017).

[4] M. Tomé and H. D. Rosales, Phys. Rev. B **103**, L020403 (2021).

[5] S. Nakatsuji, N. Kiyohara, and T. Higo, Nature (London) **527**, 212 (2015).

[6] A. K. Nayak, J. E. Fischer, Y. Sun, B. Yan, J. Karel, A. C. Komarek, C. Shekhar, N. Kumar, W. Schnelle, J. Kübler *et al.*, Sci. Adv. **2**, e1501870 (2016).

[7] H. Chen, Q. Niu, and A. H. MacDonald, Phys. Rev. Lett. **112**, 017205 (2014).

[8] J. Kübler and C. Felser, Europhys. Lett. **108**, 67001 (2014).

[9] Y. Zhang, Y. Sun, H. Yang, J. Železný, S. P. P. Parkin, C. Felser, and B. Yan, Phys. Rev. B **95**, 075128 (2017).

[10] O. Busch, B. Göbel, and I. Mertig, Phys. Rev. Research **2**, 033112 (2020).

[11] S.-S. Zhang, H. Ishizuka, H. Zhang, G. B. Halász, and C. D. Batista, Phys. Rev. B **101**, 024420 (2020).

[12] I. Martin and C. Batista, Phys. Rev. Lett. **101**, 156402 (2008).

[13] S. Zhang, M. Kang, H. Huang, W. Jiang, X. Ni, L. Kang, S. Zhang, H. Xu, Z. Liu, and F. Liu, Phys. Rev. B **99**, 100404(R) (2019).

[14] K. Ohgushi, S. Murakami, and N. Nagaosa, Phys. Rev. B **62**, R6065 (2000).

[15] L. Balents, Nature (London) **464**, 199 (2010).

[16] Y. Zhang, Y.-W. Tan, H. L. Stormer, and P. Kim, Nature (London) **438**, 201 (2005).

[17] C. L. Kane and E. J. Mele, Phys. Rev. Lett. **95**, 226801 (2005).

[18] H.-M. Guo and M. Franz, Phys. Rev. B **80**, 113102 (2009).

[19] L. Zheng, L. Feng, and W. Yong-Shi, Chin. Phys. B **23**, 077308 (2014).

[20] Z. Liu, Z.-F. Wang, J.-W. Mei, Y.-S. Wu, and F. Liu, Phys. Rev. Lett. **110**, 106804 (2013).

[21] E. Tang, J.-W. Mei, and X.-G. Wen, Phys. Rev. Lett. **106**, 236802 (2011).

[22] Y. Gao, Y.-Y. Zhang, J.-T. Sun, L. Zhang, S. Zhang, and S. Du, Nano Res. **13**, 1571 (2020).

[23] T. Moriya, Phys. Rev. **120**, 91 (1960).

[24] T. Fukui, Y. Hatsugai, and H. Suzuki, J. Phys. Soc. Jpn. **74**, 1674 (2005).

[25] D. Vanderbilt, *Berry Phases in Electronic Structure Theory: Electric Polarization, Orbital Magnetization and Topological Insulators* (Cambridge University Press, Cambridge, 2018).

[26] R.-X. Zhang, H.-C. Hsu, and C.-X. Liu, Phys. Rev. B **93**, 235315 (2016).

[27] W. Fang, A. Raeliarijaona, P.-H. Chang, A. A. Kovalev, and K. D. Belashchenko, Phys. Rev. Materials **5**, 054401 (2021).

[28] A. Zorko, M. Pregelj, A. Potočnik, J. van Tol, A. Ozarowski, V. Simonet, P. Lejay, S. Petit, and R. Ballou, Phys. Rev. Lett. **107**, 257203 (2011).

[29] N. Qureshi, A. Bombardi, S. Picozzi, P. Barone, E. Lelièvre-Berna, X. Xu, C. Stock, D. F. McMorrow, A. Hearmon, F. Fabrizi, P. G. Radaelli, S. W. Cheong, and L. C. Chapon, Phys. Rev. B **102**, 054417 (2020).